Self-Assembly of Dendrimer-Encapsulated Nanoparticle Arrays Using 2-D Microbial S-Layer Protein Biotemplates

Sonny. S. Mark,*[,†] Magnus Bergkvist,[†,‡] Xin Yang,[§] Esther R. Angert,[†] and Carl A. Batt[§]

Department of Microbiology and Department of Food Science, Cornell University, Ithaca, New York 14853

Received March 30, 2006; Revised Manuscript Received April 14, 2006

We investigated the formation of self-assembled two-dimensional (2-D) arrays of dendrimer-encapsulated platinum nanoparticles (Pt-DENs) using prokaryotic surface-layer (S-layer) proteins as biomacromolecular templates. The Pt-DENs (mean core diameter 1.8 ± 0.5 nm) were synthesized by chemical reduction of metal ion species complexed within the interior of fourth-generation, hydroxyl-terminated, starburst poly(amidoamine) dendrimers (G4 PAMAM-OH). Detailed structural and elemental composition analyses performed using high-resolution transmission electron microscopy, energy-dispersive X-ray spectroscopy, electron energy loss spectroscopy, and X-ray photoelectron spectroscopy indicated that the dendrimer−metal nanocomposite particles were crystalline in nature rather than amorphous and that at least some quantity of the platinum found within the particles is present in the expected zerovalent state. By using the S-layer lattices from the acidothermophilic archaeon *Sulfolobus acidocaldarius* and the Gram-positive bacterium *Deinococcus radiodurans* as a biotemplate, hexagonal- and honeycomb-ordered arrays of the Pt-DENs were successfully fabricated under a range of different pH conditions via noncovalent nanoparticle−protein interactions. Fast Fourier transform analyses of transmission electron microscopy images verified that the fabricated Pt-DEN assemblies displayed mean periodicities that corresponded well with the lattice constants of the native protein templates (i.e., 22 and 18 nm for *S. acidocaldarius* and *D. radiodurans* S layers, respectively). Our results demonstrate that utilizing pre-synthesized Pt-DENs in conjunction with microbial S-layer proteins displaying highly periodic topochemical properties can be an effective, novel route for creating patterned arrays of Pt nanoparticles with potential technological applications.

1. Introduction

The controlled organization of colloidal nanoparticles into ordered array structures with interesting physical and chemical properties is expected to be a crucial component for the development of functional nanoscale devices having applications in a number of diverse areas such as molecular electronics,[1] photonics,[2] electrocatalysis,[3] and chemical sensing/biosensing.[4] Consequently, there has been an increased level of interest in recent years in the development of effective strategies for the "bottom-up" synthesis of linear and planar arrays of a wide range of technologically important materials such as gold nanoparticles, CdSe quantum dots, and other types of metallic/semiconducting nanocrystals.

Current methods to prepare 2-D arrays of nanostructured materials include laser ablation,[5] spin coating of sol gel solutions onto substrate materials followed by high-temperature calcinations,[6] thermal decomposition of transition metal carbonyls,[7] photolithography,[8] electron-beam lithography,[9] and scanning probe lithography (SPL).[10] However, all of the methods listed above have significant deficiencies: (1) nonlithography methods, although they are routinely able to access the nanoscale regime (1−100 nm), do not permit precise and reproducible control over the size and surface structure of the nanoparticle features, (2) the resolution of conventional photolithography methods is typically limited by optical diffraction effects, making the fabrication of feature sizes below 100 nm extremely challenging, and (3) the serial nature of EBL and SPL makes them relatively slow and costly. One promising alternative approach to the advanced fabrication of ordered nanostructures is the application of biological molecules such as DNA and proteins as synthetic templates.[11,12] In particular, the nanometric spatial modulation of the inherent physicochemical and morphological properties of surface-layer (S-layer) proteins[13,14] makes them an ideal type of matrix for biotemplating the direct chemical synthesis of inorganic nanocluster arrays. Previous studies have shown, for example, that the direct nucleation and growth of metal clusters on S-layer templates[15−17] can lead to metallo-organic nanostructures with feature densities exceeding those found in the current generation of microelectronic processors.[18] On the other hand, most of the experimental results that have been reported to date clearly indicate that the metal precipitation/electroless deposition (ELD) techniques typically employed in such types of protein-based, in situ array bionanofabrication procedures do not easily permit fine control over particle size and morphology, important parameters for achieving the synthesis of high-quality, uniform nanoarrays.

In this article, we describe a novel, alternative process for patterning nanostructured arrays on S layers using preformed nanoparticles synthesized within dendrimer molecules. Poly(amidoamine) (PAMAM) "starburst" dendrimers,[19−21] first discovered and synthesized by Tomalia and co-workers in the late 1970s, are chemically versatile organic macromolecules with an intrinsically well-defined globular structure (see the Supporting Information, Figure S1) which have been shown to be ideal host molecules for the aqueous, surfactant-free synthesis of metallic and semiconducting nanoparticles.[22−24] Inorganic clusters grown within dendrimers are typically spherical in shape

* Corresponding author. Phone: 607 255-7902. Fax: 607 255-8741. E-mail: ssm12@cornell.edu.

† Department of Microbiology, Cornell University.

‡ Present Address: Nanobiotechnology Center at Cornell University, Ithaca, New York 14853.

§ Department of Food Science, Cornell University.

10.1021/bm0603185 CCC: $33.50
Published on Web 05/12/2006

and are stabilized by the highly regular three-dimensional network of branches comprising the interior of these polymeric macromolecules. One important advantage of using dendrimeric templates is that the final dimensions of the synthesized nanoparticles can be controlled by varying the dendrimer physical size (generation) and the metal ion loading quantity.[25] Moreover, the exterior surfaces of dendrimers have numerous functional groups that can potentially provide reactive/derivatizable handles for linking nanoparticles to solid substrates and other types of structures.[26]

As first demonstrated by Crooks and co-workers,[27,28] dendrimers containing terminal hydroxyl groups (PAMAM-OH) are particularly well-suited for the synthesis of nanoparticles since (i) they are water-soluble and (ii) the exterior hydroxyl functional groups are noncomplexing toward most species of metal ions. This latter property is of practical significance, since dendrimers terminating with efficient metal ligand groups often become cross-linked in the presence of metal ions and precipitate out of solution.[29] Thus, in this work, we carried out the synthesis, characterization, and surface immobilization of platinum nanoparticles encapsulated within fourth-generation, hydroxyl-terminated PAMAM dendrimers. Nanostructured platinum was chosen as a model metal for this work since it is of interest for a broad range of technological applications, including sensors[30] and other devices.[31] In particular, ordered platinum nanoparticle arrays are expected to serve as useful model systems[32,33] for studying the effects of surface structure on catalyst performance in industrially important applications such as low-temperature fuel cells[34] and catalytic converters for emissions controls.[35]

Given the significant level of interest in their potential technological applications, the synthesis of nanostructured films containing monolayers of PAMAM dendrimers or dendrimer-encapsulated nanoparticles on various types of surfaces has been actively investigated by a few groups. The most commonly employed approaches have relied on strategies such as covalent linkage[36−40] and electrostatic attachment.[41] Typically, in both of these methods, the final result obtained is either the random (i.e., nonpatterned), bulk deposition of the individual dendrimer-based components on the substrate surface or the creation of particle films with only a very limited degree of 2-D ordering. Recently, for example, Liu et al. demonstrated that the electrostatic complexation of PAMAM-NH_2 dendrimer-encapsulated gold nanoparticles with DNA in aqueous solution led to the formation of "pearl-chain" nanowires.[42] However, when drop-casted onto a mica substrate, atomic force microscopy (AFM) analyses revealed that the packing of the surface-immobilized nanowire chains lacked any significant long-range positional order. In an alternative approach, the fabrication of dendrimer-containing thin film structures using a combination of electrostatic- and hydrogen bonding-based interactions was reported by Zhong et al.[43] In their work, multilayer ultrathin films were successfully obtained on quartz wafer substrates by using phenolic shell-modified generation 3 dendrimers and a diazo resin (DR) compound as building blocks in a layer-by-layer (LBL) self-assembly technique.

Here we produce 2-D patterned arrays of dendrimer-encapsulated platinum nanoparticles (Pt-DENs) by exploiting the *Deinococcus radiodurans* and *Sulfolobus acidocaldarius* S layers as a nanoarchitectural biotemplate (see Figure 1 for a schematic illustration of the procedure). We selected the native S-layer structures from *D. radiodurans* and *S. acidocaldarius* as model systems since they can be purified relatively easily, and both types of S layers are able to withstand long periods of storage (i.e., >6 months) at 4 °C without any noticeable morphological degradation.[44] The *D. radiodurans* S layer, also known as the hexagonally packed intermediate (HPI) layer, has a p6 rotational symmetry with a reported spacing of 18 nm between each protein core region[45] (Figure 2A). Recent investigations have shown that the HPI S layer can specifically bind citrate-capped gold nanoparticles, resulting in ordered arrays spanning over several hundred nanometers.[46,47] The *S. acidocaldarius* S layer (referred to herein as "SAS" or "SAS S layer") displays a p3 symmetry structure with a reported lattice constant of 22 nm[48] (Figure 2B). The overall symmetry structure across the 2-D SAS crystal can be regarded as being hexagonal, similar to the HPI S layer.

In our bionanofabrication scheme, Pt-DENs are first prepared in aqueous solution using a template approach in which platinum metal ion complexes are sequestered within hydrophilic generation 4 PAMAM-OH dendrimers (theoretical diameter = 4.5 nm)[49] and then chemically reduced with sodium borohydride. Preliminary characterizations of the synthesized Pt-DEN particles were performed using transmission electron microscopy (TEM), energy dispersive spectroscopy (EDS), electron energy loss spectroscopy (EELS), and X-ray photoelectron spectroscopy (XPS). Following the nanoparticle characterization steps, we generated self-assembled arrays of Pt-DENs on the S layers via a spontaneous adsorption process driven by noncovalent interactions. The morphological ordering of the resulting nanoparticle arrays was investigated using TEM and image processing techniques. Finally, the influence of solution pH was also examined in order to determine the optimal conditions for the formation of the S-layer-biotemplated Pt-DEN arrays. To our knowledge, this work represents the first demonstration of the guided self-assembly of long-range ordered, 2-D arrays of dendrimer-encapsulated monometallic nanoparticles using a protein-based nanobiological template.

2. Experimental Section

2.1. Materials. 2.1.1. Reagents and Other Chemicals. Disodium hydrogen phosphate (Na_2HPO_4), sodium dihydrogen phosphate (NaH_2PO_4), potassium tetrachloroplatinate(II) (K_2PtCl_4), sodium borohydride ($NaBH_4$), and generation 4 poly(amidoamine) dendrimers with 64 surface hydroxyl groups (G4 PAMAM-OH; see Figure S1) (10% w/w in methanol) were purchased from Aldrich Chemical Co. (Milwaukee, WI). Unless stated otherwise, all reagents and chemicals (ACS grade or better) were purchased either from Aldrich Chemical Co. or from Sigma Chemical Co. (St. Louis, MO) and used as received. All aqueous solutions were prepared by using reagent grade (18 MΩ cm resistivity) deionized water (DI H_2O) purchased from Stephens Scientific Co. (Riverdale, NJ). Prior to use in synthesis experiments, the PAMAM-OH dendrimer was rotovaped to remove the methanol solvent and resuspended in DI H_2O to give a 1 mM aqueous stock solution. Solutions containing $NaBH_4$ were made up fresh for each synthesis. All glassware was cleaned using PCC-54 detergent solution from Pierce Biotechnology, Inc. (Rockford, IL) and rinsed thoroughly with DI H_2O.

2.1.2. Dialysis Units. For the purification of nanoparticle synthesis products, we used Slide-A-Lyzer MINI dialysis microtubes from Pierce Biotechnology, Inc. The dialysis units contain a regenerated cellulose membrane having a nominal molecular weight cutoff (NMWCO) of 3500 MW. Based on simple assumptions for a "typical" globular protein model [i.e., $\text{volume}_{\text{protein}}\ (\text{nm}^3) = (\text{MW}_{\text{protein}}\ (\text{g mol}^{-1}) \times 0.73\ \text{cm}^3\ \text{g}^{-1} \times 10^{21}\ \text{nm}^3\ \text{cm}^{-3})/(6.02 \times 10^{23}\ \text{mol}^{-1})$], this NMWCO value roughly corresponds to a physical membrane pore diameter of approximately 2 nm. A relatively small NMWCO value was chosen in order to prevent losses of the PAMAM-OH dendrimer-encapsulated nanoparticles (DENs) during the dialysis period.

2.2. Cell Culture Conditions and Purification of S-Layer Proteins. Growth of *Deinococcus radiodurans* strain Sark I and extraction of

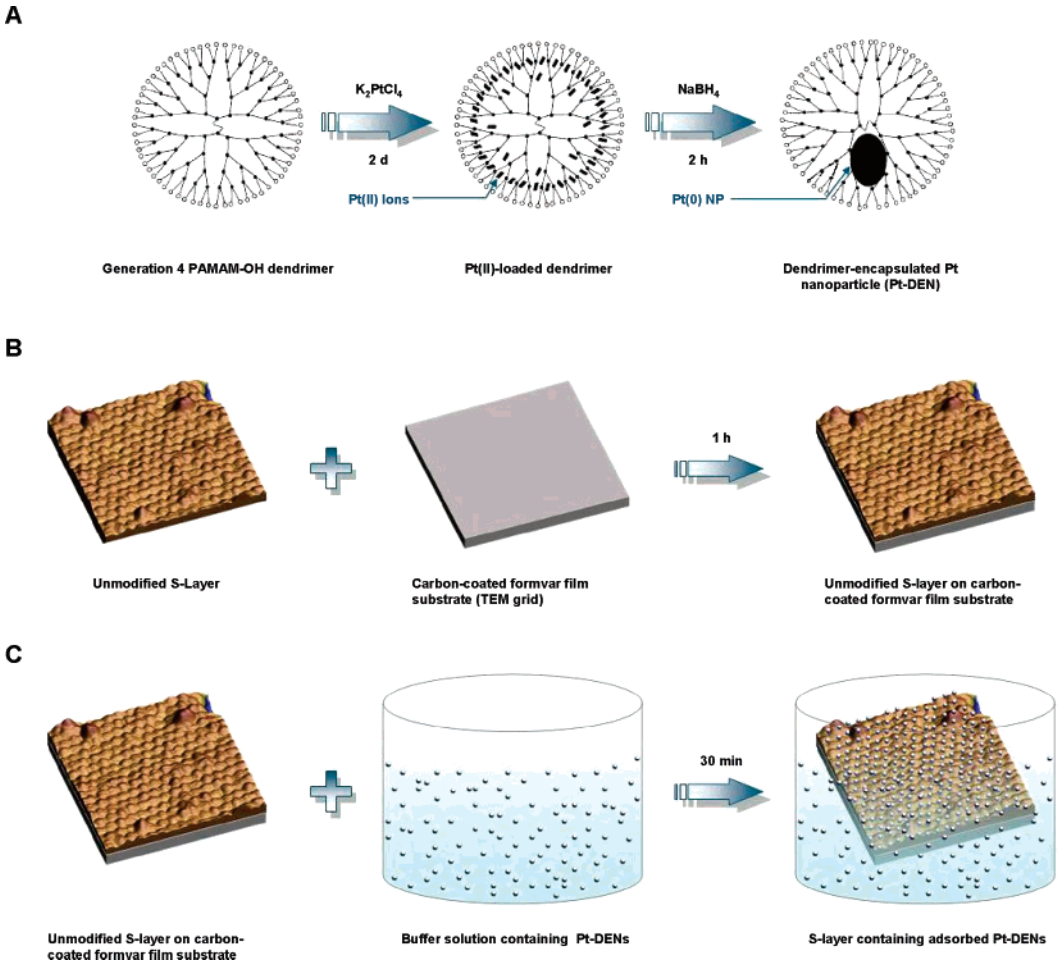

Figure 1. Schematic illustration of the synthesis of dendrimer-encapsulated platinum nanoparticles (Pt-DENs) and their adsorption onto an S-layer biotemplate. A. Synthesis of platinum metal nanoparticles within a generation 4 hydroxyl-terminated poly(amidoamine) (G4 PAMAM-OH) dendrimer template. The nanocomposite materials are prepared by mixing an aqueous solution of the dendrimer and metal ion, and subsequent chemical reduction. B. Adsorption of S layers onto transmission electron microscopy (TEM) grid substrates containing a carbon-coated Formvar film. C. Adsorption of Pt-DENs (in buffered aqueous solution) onto immobilized S layers.

HPI S-layer protein fragments were performed as described previously.[47] *Sulfolobus acidocaldarius* strain DG6 was obtained from the American Type Culture Collection (ATCC No. 49426) and grown aerobically in batch culture in ATCC medium 1723 (pH 3.0) at 75 °C. Upon reaching an optical density at 600 nm between 0.5 and 0.6, the cell culture was neutralized with solid $NaHCO_3$. The cells were then harvested by centrifugation at 3500*g* for 30 min at 4 °C. After the initial centrifugation step, the cell pellets were resuspended in SAS S-layer isolation buffer (10 mM HEPES, 2.0 mM Na_2·EDTA·H_2O, 0.5 mM 4-(2-aminoethyl) benzenesulfonyl fluoride (AEBSF), pH 7.0). The extraction of SAS S-layer sheets from the cells was performed according to the procedure originally described by Michel et al.[50] To break the SAS sacculi into monolayer fragments suitable for nanoparticle binding experiments, the protein solution was sonicated on ice using a Branson Ultrasonics (Danbury, CT) model 250 Sonifier equipped with a 3.2 mm microtip probe (10 s, continuous duty cycle, 100 W). Both the HPI and SAS S-layer stock solutions were adjusted to give a working protein concentration of 50 μg mL^{-1} in DI H_2O and stored at 4 °C until further use

2.3. Synthesis of Dendrimer-Encapsulated Platinum Nanoparticles. The synthesis and purification of PAMAM-encapsulated platinum nanoparticles (Pt-DENs) were performed similarly to procedures originally developed by Crooks and co-workers.[27] Briefly, 0.5 mL of 1 mM PAMAM-OH stock solution was added to 10 mL of 3 mM aqueous K_2PtCl_4 and stirred for 2 days. The resulting solution contained a nominal metal ion-to-dendrimer ratio of 60:1. Reduction of the solution containing G4 PAMAM-OH(Pt^{2+}) complexes was achieved by adding 150 μL of fresh 1.5 M aqueous $NaBH_4$ (a 7.5:1 molar ratio of $NaBH_4$ to Pt^{2+} ions) and stirring for 2 h at room temperature (20 °C). Following a low-speed (1500*g*) centrifugation step to remove any precipitated material, the product solutions were purified by dialysis against DI H_2O. A standard dialysis regimen entailed the use of 4000 mL of DI H_2O per 100 μL of sample, with three changes of water per day for a minimum of 2 days. A control synthesis reaction was prepared similarly, but with DI H_2O substituting for the G4 PAMAM-OH solution.

2.4. Biotemplating of Nanoparticles on S−Layers. For the nanoparticle binding experiments, plasma-cleaned carbon-coated Formvar TEM grids were floated on top of 50-μL drops of the S-layer solution (50 μg mL^{-1} in DI H_2O) for 1 h and then rinsed by floating each grid on three separate 50-μL drops of DI H_2O (30 s each wash). Immediately after the rinsing steps, each grid (now coated with S-layer protein) was floated onto a 50-μL drop of 0.01 mM Pt-DENs in 20 mM sodium phosphate buffer (pH 5, 7, or 9). After 30 min, rinsing steps in DI H_2O were performed similarly as before to remove loosely adsorbed nanoparticles. Finally, the samples were blot-dried using filter paper and imaged by transmission electron microscopy.

2.5. Instrumentation. 2.5.1. Ultraviolet−Visible Absorption Spectroscopy. UV−vis spectra were acquired at room temperature using an Ultrospec II spectrophotometer (Amersham Biosciences, NJ) between 200 and 600 nm in 1-cm quartz cuvettes with a resolution of 0.5 nm. For all UV−vis spectroscopy measurements, the sample solutions were diluted 10-fold in DI H_2O.

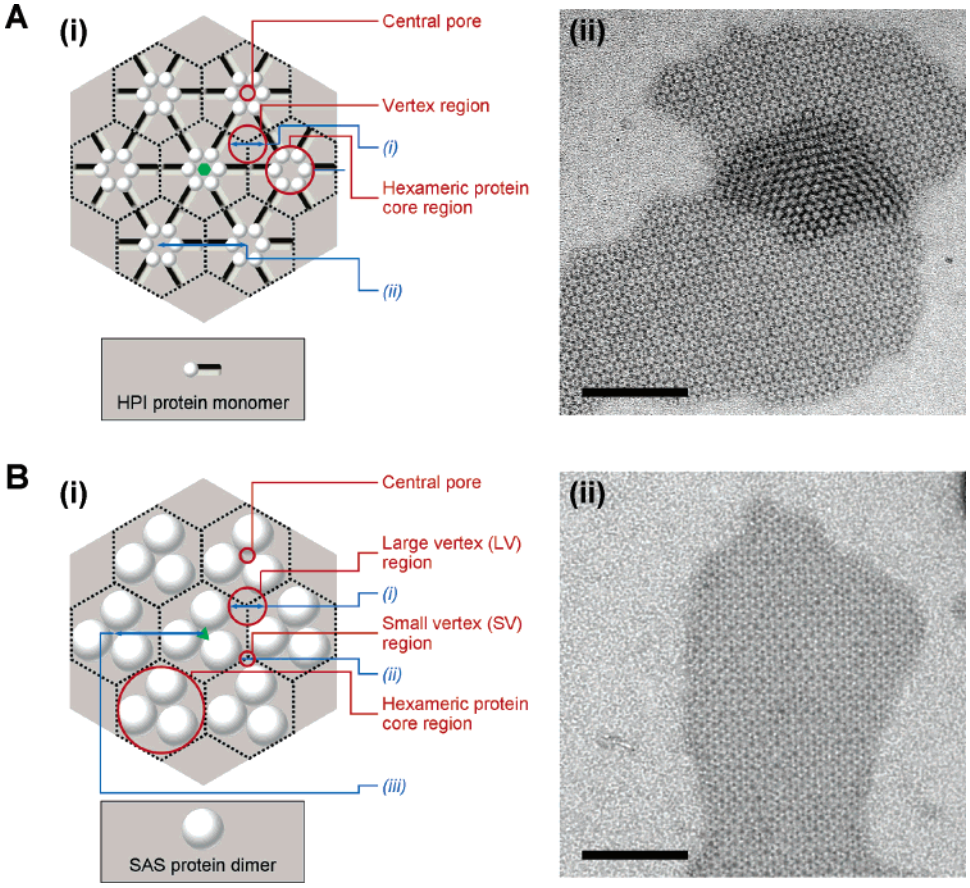

Figure 2. Comparison of the HPI and SAS S-layer protein lattice structures. In the schematic drawings, black dotted lines illustrate a regular hexagonal lattice model overlaid on top of each S-layer lattice such that (1) the corners of the hexagons correspond to the vertex regions and (2) the geometric center of each hexagon corresponds to the location of the central pore. The protein lattice structures are not drawn to scale. A. (i) Structure of the HPI S layer (p6 symmetry). In each (hexameric) core region, six protein monomers surround a central pore. Each core region is in turn surrounded by six identical vertex regions. The vertex regions are arranged in a 6-fold symmetric pattern with the axis of symmetry (green solid hexagon) located at the central pore. Spoke-like protrusions emanate from each monomer to connect adjacent hexameric clusters. Blue double-headed arrows indicate the following dimensional parameters for the native HPI S-layer structure:[44] (i) diameter of the vertex region (7.1 ± 0.5 nm); and (ii) spacing between adjacent core regions ("HPI lattice constant") (18.5 ±0.7 nm). (ii) Brightfield TEM image of native HPI S-layer protein lattices. The image shows two S-layer fragments that are partially overlapping with each other. B. (i) Structure of the SAS S layer (p3 symmetry). In each (hexameric) core region, three protein dimers surround a central pore. Each core region is in turn surrounded by three identical large vertex (LV) regions and three identical small vertex (SV) regions. The LV and SV regions are arranged in a 3-fold symmetric pattern with the axis of symmetry (green solid triangle) located at the central pore. Blue double-headed arrows indicate the following dimensional parameters for the native SAS S-layer structure:[44] (i) diameter of the LV region (11.4 ± 0.5 nm); (ii) diameter of the SV region (5.6 ± 0.4 nm); and (iii) spacing between adjacent core regions ("SAS lattice constant") (21.6 ± 0.8 nm). (ii) Brightfield TEM image of a native SAS S-layer protein lattice fragment. For all TEM images, scale bar = 200 nm. All S-layer dimensional measurements are those reported previously by Mark et al.[44]

2.5.2. Electron Microscopy. Transmission electron microscopy (TEM) was performed using a Morgagni 268 transmission electron microscope (Philips/FEI Company, OR) operated at an accelerating voltage of 80 kV. High-resolution TEM (HRTEM) analysis of the Pt-DENs was performed using an FEI Tecnai TF20 field emission gun (FEG) transmission electron microscope operated at 200 kV. The Tecnai TF20 instrument permits high-resolution imaging with a point-to-point resolution of ~1.6 Å. For TEM and HRTEM analyses of the Pt-DENs without any S layers, the (unstained) samples were prepared by placing a 3-μL drop of nanoparticle solution (diluted 10-fold in DI H_2O) onto a holey-carbon/ultrathin carbon-coated copper (Cu) TEM grid (Ted Pella, Inc., CA) and then allowing the solution to dry. After briefly rinsing in DI H_2O, excess liquid was removed with filter paper and the grids were air-dried. Samples of native S-layer proteins (without Pt-DENs) were adsorbed onto carbon-coated Formvar Cu TEM grids and negatively stained for 1 min with a methylamine tungstate stain (Nanoprobes, NY) prior to TEM imaging. Samples containing Pt-DENs adsorbed onto S-layer protein fragments pre-immobilized on carbon-coated Formvar Cu TEM grids were imaged directly without any staining. Prior to sample deposition, all TEM grids were cleaned for 1 min at high power (29.6 W) in a benchtop air plasma cleaner (Harrick Scientific, NY).

2.5.3. Energy Dispersive X-ray Spectroscopy. EDS spectra of the Pt-DENs adsorbed onto clean silicon (100) wafer substrates were acquired using a GENESIS 2000 X-ray Microanalysis System (EDAX, Inc., NJ) mounted on a Zeiss Ultra 55 field emission scanning electron microscope (SEM) (Carl Zeiss MicroImaging, Inc., NY). The accelerating voltage used for the EDS analyses was 20 kV, and the working distance was maintained at 10 mm. The EDS spectrometer system was calibrated using the Al Kα and Cu Kα lines. Representative EDS spectra obtained by scanning a region of interest 1 × 1 μm in size are presented.

2.5.4. Electron Energy Loss Spectroscopy. EELS spectra of Pt-DEN samples adsorbed onto ultrathin carbon/holey carbon copper TEM grids were acquired using a model HB501A ultrahigh vacuum scanning transmission electron microscope (UHV−STEM) (VG Scientific, U.K.) equipped with a parallel electron energy loss spectrometer (PEELS) system. The probe size used for the EELS analyses was ~0.3 nm, and the accelerating voltage was fixed at 100 kV. The effective energy resolution of the VG-HB501A field emission instrument is ~0.8 eV. The measured position of the C K (1s) peak at 284.9 eV (arising from

transitions to the π^* molecular orbital) from the TEM carbon film support material was used to evaluate the energy calibration. Representative EELS spectra obtained by scanning a region of interest 10.5 × 14 nm in size are presented.

2.5.5. X-ray Photoelectron Spectroscopy. XPS spectra were acquired using an Axis Ultra spectrometer (Kratos Analytical Inc., NY) equipped with a monochromatized Al Kα X-ray radiation source (photon energy 1486.6 eV). To perform the analyses, the Pt-DENs were adsorbed onto clean silicon substrates. During analysis, the pressure inside the chamber was held below 2×10^{-8} Torr and a takeoff angle of 90° was used for all measurements. The energy resolution of the spectrometer instrument was ~0.15 eV. To compensate for surface charging effects, all binding energies were referenced with respect to the C 1s peak energy of 284.6 eV.

2.6. Image Processing and Data Analysis. 2.6.1. Mean Particle Size/Coverage Determination. Real-space statistical analyses of nanoparticle dimensions were performed on TEM images of unstained Pt-DENs using ImageJ, a JAVA-based software developed by the National Institutes of Health (NIH) (http://rsb.info.nih.gov/ij/). The particle size measurements presented are mean values (± standard deviation) calculated from a minimum of 500 measurements obtained from different areas of the sample. For the biotemplating experiments, nanoparticle surface coverage measurements were carried out by first defining a region of interest (ROI) on the S layer and then performing a threshold/grain analysis of TEM images using ImageJ to quantitate the number of particles per square micrometer. Surface coverage data presented are mean (± standard deviation) values calculated from a minimum of 4 nonoverlapping ROIs (sample area size for each ROI = 238 × 238 nm).

2.6.2. X-ray Photoelectron Spectra Analysis. The high-resolution XPS data were smoothed using a (second order) Savitzky-Golay algorithm and fitted to linear combinations of individual components using the spectra deconvolution software program XPSPEAK 4.1 (freely available at: http://www.phy.cuhk.edu.hk/~surface/XPSPEAK/) written by R. W. M. Kwok, Chinese University of Hong Kong, HK. Correction for background noise was performed using the software's built-in spectrum background subtraction method (based on a combination of Shirley[51] and linear functions). The Pt 4f line for elemental platinum is known to be a doublet with the components Pt $4f_{5/2}$ and Pt $4f_{7/2}$ being separated in energy by 3.3 eV[52] and having a theoretical integrated peak area ratio ($area_{Pt\ 4f5/2}/area_{Pt\ 4f7/2}$) of 0.75.[53] Therefore, all Pt 4f curves were fitted similarly using the above constraints for elemental platinum. During the curve fitting process, the following parameters of the component peaks were allowed to vary: binding energy (BE), peak area, full width at half-maximum (fwhm), and the Gaussian−Lorentzian peak line shape[54] mixing ratio. No tailing function was considered in the peak fitting procedure. The components of the various spectra were mainly modeled as symmetrical Gaussian peaks unless a certain degree up to 52% of Lorentzian shape was necessary for the best fit. The fwhm value for each of the various components of a given spectrum were kept as close as possible with a difference up to ±0.4 eV. A goodness-of-fit statistical parameter, the reduced chi-square (χ^2),[55] was used to determine the quality of the fit in terms of representing the XPS data. The reduced chi-square is the sum of the squares of the difference between the experimental spectrum and the fitted envelope at each point over the peak region of interest, divided by the variance. In practice, a reduced chi-square value of less than or equal to 2 is typically regarded as indicative of an acceptable peak-fit.[56] A chi-square value between 2 and 4 implies that the fit has not yet been optimized. Finally, a chi-square value larger than 4 implies that one or more signals may be missing from the peak-fitting effort. In our curve fitting procedure, we iteratively increased the number of individual (hypothetical) peaks until a reduced chi-square value less than or equal to 2.0 was obtained, thereby achieving good fit quality with the minimum number of statistically justifiable peaks.

2.6.3. Fourier Transform Analysis. 2-D fast Fourier transforms (FFT)[57] of TEM images of the biotemplated nanoparticles were analyzed using the Digital Micrograph 3.1 software program (Gatan, CA) in order to determine the orientational symmetry of the peak reflections, and to derive the major lattice line spacing values (*d*-spacings; see Figure S3 in the Supporting Information) in the real-space lattice structure. For the FFT analyses, a circular region of interest (diameter = 400 pixels) for each nanoparticle array image was digitally selected and then floated into a blank square area (512 × 512 pixels) using Paint Shop Pro 8.0 software (Corel, MN).

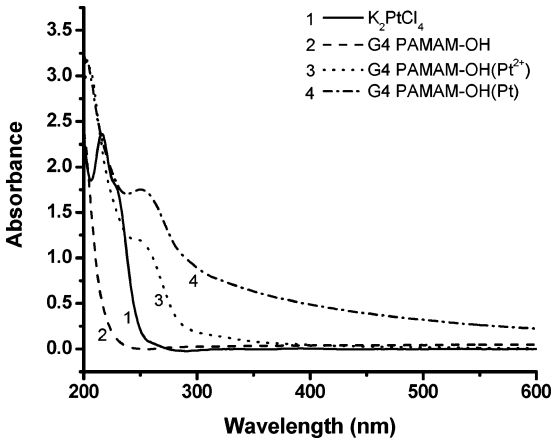

Figure 3. UV−vis absorption spectroscopy demonstrating sorption of Pt^{2+} ions into G4 PAMAM-OH dendrimers and subsequent chemical reduction to yield dendrimer-encapsulated platinum nanoparticles. 1. 3 mM K_2PtCl_4 solution. 2. 0.05 mM G4 PAMAM-OH dendrimer. 3. Solution containing 3 mM K_2PtCl_4 and 0.05 mM G4 PAMAM-OH dendrimer before reduction with $NaBH_4$. 4. Solution containing 3 mM K_2PtCl_4 and G4 PAMAM-OH dendrimer after reduction with $NaBH_4$.

3. Results and Discussion

3.1. Pt G4 PAMAM-OH Synthesis and Characterization. Pt DENs were prepared similarly to published procedures[27,28] by stirring aqueous solutions containing G4 PAMAM-OH and K_2PtCl_4 for 2 days and then reducing the Pt^{2+} metal ion complexes with $NaBH_4$. (In this work, we henceforth refer to all of the possible forms of platinum-related aqueous complex ions present in the solution phase and within the dendrimer interior space as "Pt^{2+} ion species.") The final solution containing the Pt DENs was purified by dialysis for a minimum of 48 h against pure DI H_2O using regenerated cellulose tubing with a 3500 MW cutoff.

During the nanoparticle preparation process, changes in sample absorption properties were recorded using a UV−vis spectrophotometer. Figure 3 shows UV−vis absorbance spectra of K_2PtCl_4, PAMAM-OH, and solutions of G4 PAMAM-OH dendrimers containing Pt^{2+} ions (G4 PAMAM-OH(Pt^{2+})) obtained over a 2-day period before as well as after reduction (2 h) with $NaBH_4$. The characteristic feature found in the spectrum plot for a freshly prepared solution of K_2PtCl_4 in the absence of dendrimer is the strong absorption band at 215 nm. This relatively intense signal can be ascribed to ligand-to-metal charge transfer (LMCT) transitions[27] involving the movement of electrons from a predominantly (Cl^- ion-based) ligand orbital to a predominantly (Pt^{2+} ion-based) metal orbital. The absorption spectrum of an aqueous solution of G4 PAMAM-OH dendrimers, on the other hand, is essentially featureless and shows only a monotonic increase toward higher energy. Upon addition of PAMAM-OH dendrimers to the K_2PtCl_4 solution (nominal dendrimer:platinum molar ratio of 1:60), the band at 215 nm decreases and a new UV−vis band at 250 nm emerges. These changes are a consequence of the encapsulation of metal ion

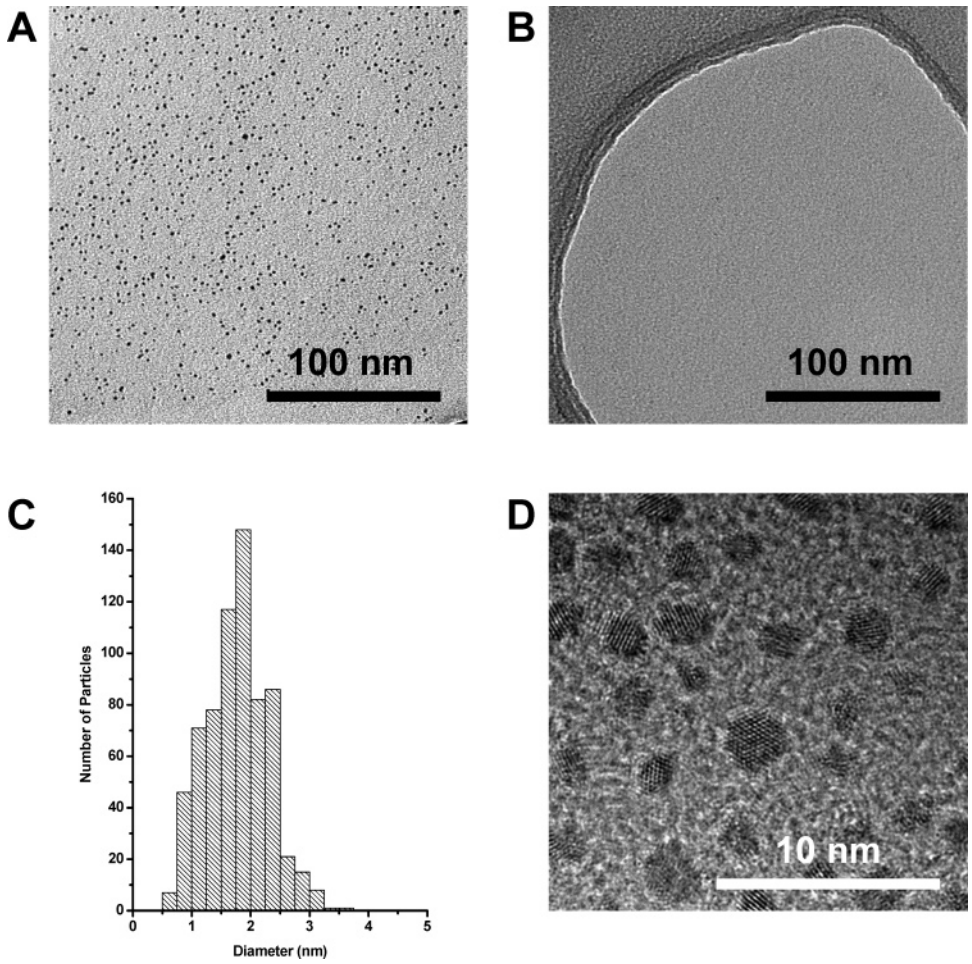

Figure 4. Bright field transmission electron microscopy (TEM) and size distribution analysis of dendrimer-encapsulated platinum nanoparticles (Pt-DENs). A. Overview TEM image of a sample taken from a Pt-DEN synthesis reaction and dialyzed in DI H_2O for 48 h. Nanoparticles are visibly distributed throughout the image. B. Overview TEM image a sample taken from a control nanoparticle synthesis reaction carried out without any PAMAM-OH dendrimer template present and dialyzed in DI H_2O for 48 h. No nanoparticles are visible. Note that the speckled appearance of the holey carbon/ultrathin carbon film support structure (dark gray region) is plainly visible. C. Size distribution plot for a Pt-DEN sample obtained after dialysis in DI H_2O for 48 h. D. High-resolution TEM image of the synthesized Pt-DENs.

complexes by the dendrimer molecules.[27] In particular, the new peak at 250 nm can be attributed to the complexation of Pt^{2+} ion species to the interior tertiary amines of the G4 PAMAM-OH dendrimer.[29,58]

Chemical reduction of the aqueous G4 PAMAM-OH(Pt^{2+}) complexes with excess $NaBH_4$ produced a solution containing G4 PAMAM-OH(Pt) nanocomposite particles (referred to herein as "Pt-DENs"). Figure 3 shows the UV−vis absorbance spectrum of the Pt-DEN solution 2 h after reduction. The broad, essentially featureless absorption at lower-energy wavelengths >300 nm is consistent with the formation of colloidal platinum[22] and results from the interband transitions of electrons from the highest occupied valence band into the lowest unoccupied conduction band of the encapsulated zerovalent metal particles.

Transmission electron microscopy (TEM) analyses of dialyzed, unstained Pt-DENs adsorbed onto holey carbon/ultrathin carbon-coated support grids confirmed that chemical reduction of Pt^{2+} complexes encapsulated within the G4 PAMAM-OH dendrimers produced well-dispersed nanoparticles (Figure 4A). When we analyzed the dialyzed products of a control synthesis reaction, conducted without any dendrimer reagent present, no nanoparticles were observed on the TEM grids (Figure 4B). The absence of any visible nanoparticles in TEM images of the control sample is fully consistent with our supposition that reduction of the K_2PtCl_4 salt solution in the absence of any PAMAM dendrimers mainly resulted in the production of extremely fine water soluble particles that were mostly removed during the subsequent dialysis purification step. As is evident from Figure 4A, most of the dendrimer-encapsulated particles are spheroidal in shape. A size distribution analysis of the particles reveals that they are nearly monodisperse, with a mean particle diameter of 1.8 ± 0.5 nm (Figure 4C). The formation of mostly isolated, spheroidal nanoparticles demonstrates the effectiveness of using the dendrimer molecules, both as nanoreactor vessels for the preparation of relatively uniform-sized nanoparticles in a "green" solvent such as water and as nanoporous stabilizers for the prevention of aggregation.

Additional structural characterizations of the dendrimer−metal nanocomposite particles were performed using high-resolution transmission electron microscopy (HRTEM). In the HRTEM image shown in Figure 4D, the Pt-DENs, appearing as dark features due to the good electron contrast in the particle core regions, manifest distinctly visible lattice fringes indicative of crystalline order. The measured interplanar spacing is 0.22 nm for most of the particles, which is in good agreement with the (111) lattice *d*-spacing of bulk fcc platinum[59] (0.23 nm). As with the conventional, low-resolution TEM imaging mode (cf. Figure 4A), we do not expect to see the individual G4 PAMAM-OH dendrimer shells surrounding the particle cores in the HRTEM image because of the inherently low contrast of

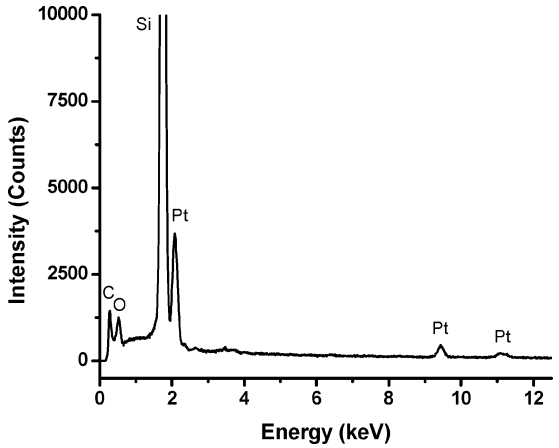

Figure 5. EDS spectrum of G4 PAMAM-OH(Pt) dendrimer-encapsulated nanoparticles. The detected peaks correspond to the following: C Kα (0.28 keV), O Kα (0.53 keV), Si Kα (1.75 keV), Pt Mα,β (2.08 keV), Pt Lα (9.43 keV), Pt $L\beta_1$ (11.08 keV), and Pt $L\beta_2$ (11.23 keV). The presence of the Si peak is due to the supporting silicon (100) wafer substrate.

the carbon (C), nitrogen (N), and oxygen (O) atoms. The observation of clearly resolved lattice fringes in the HRTEM image of the Pt-DENs produced in this work contrasts with the findings previously reported by other groups[27,28,60] which have suggested that the atoms constituting the PAMAM-OH-stabilized Pt nanoparticle cores may be in a disordered arrangement.

Elemental composition analyses were initially carried out using energy-dispersive X-ray spectroscopy (EDS) in order to verify the presence of the following in the Pt-DEN samples: (1) carbon and nitrogen (arising from the dendrimer component) and (2) platinum (from the nanoparticle core). As expected, the resulting EDS spectrum (Figure 5) shows a strong Si peak (Si Kα, 1.75 keV) arising from the supporting silicon (100) wafer substrate. Importantly, a number of peaks corresponding to platinum (Pt Mα,β, 2.08 keV; Pt Lα, 9.43 keV; Pt $L\beta_1$, 11.08 keV; and Pt $L\beta_2$, 11.23 keV) are also seen, thus clearly indicating that the nanoparticles were of the expected metallic composition. In addition, a carbon peak (C Kα, 0.28 keV) is plainly visible, consistent with the presence of an organic dendrimer scaffold surrounding the particles. The oxygen peak (O Kα, 0.53 kV) in the spectrum is likely due to both the PAMAM-OH dendrimer component in the Pt-DEN sample and the oxygen atoms present in the native oxide layer of the silicon substrate. Significantly, the EDS spectrum does not contain any obvious nitrogen (N Kα) signals. It is possible that in these samples the nitrogen peak (N Kα is expected at 0.39 keV) is simply obscured by the more dominant carbon and oxygen signals present. On the other hand, the absence of any visible N Kα signals may have also been due to the relatively poor sensitivity of the EDS technique for detecting light elements, particularly nitrogen[61] (since N Kα X-ray emissions tend to become strongly absorbed by any carbon present).

To obtain a more accurate assessment of whether the Pt-DEN samples are associated with the presence of nitrogen, we conducted further elemental composition analyses using parallel electron energy loss spectroscopy (EELS). In the dark field scanning transmission electron microscopy (STEM) images presented in Figure 6, panels A and C, the regions marked by a white box indicate the selected specimen grid areas where the EELS spectral data were collected. Each data set was collected by scanning a finely focused electron probe (~0.3 nm diameter) over a nanoscale rectangular area 10.5 × 14 nm in size. Figure 6B shows the EELS spectrum that was acquired for an area containing several isolated particles. The acquired spectrum clearly reveals the presence of the characteristic *K*-shell ionization edge of nitrogen (N) at ~399 eV. As expected, a scan of an equally sized area of the sample which contained *no* visible nanoparticles did *not* indicate the presence of the N *K* edge absorption feature (Figure 6D). The above results obtained from the EELS analyses thus provide, in a visually direct manner, strong chemical evidence that the nanoparticles synthesized in this work are indeed associated with an intrinsically nitrogen atom-rich dendrimer component.

More detailed information about the oxidation states of the platinum component in the dendrimer-encapsulated nanoparticle samples was obtained by X-ray photoelectron spectroscopy (XPS). In conducting these characterization studies, the major objective was to determine whether the platinum found within the Pt-DENs is in an elemental state (i.e., Pt^0). As shown in Figure 7A, the experimental high-resolution Pt 4f core level spectrum obtained for Pt-DENs dried on a silicon wafer substrate exhibits a doublet corresponding to the Pt $4f_{7/2}$ and Pt $4f_{5/2}$ peaks. As expected, no platinum was detected during control scans of the "blank" silicon substrate (Figure S2A). A nonlinear regression analysis of the Pt 4f spectrum shown in Figure 7A was conducted using XPSPEAK version 4.1 software. This software employs the least squares approach by introducing a fit parameter, the reduced χ^2 (chi-square), to determine the quality of the model fit. In performing the curve fitting analyses, the number of component peaks is iteratively increased until the reduced chi-square is less than or equal to 2.0, thereby achieving a good quality of fit to the data with the minimum number of statistically justifiable peaks. When using this procedure, we found that the Pt 4f spectrum can be deconvoluted into three pairs of spin−orbit doublets, each with Gaussian−Lorentzian line shapes. The pair of Pt 4f peaks at 71.7 and 75.0 eV have binding energies very close to the values of 71.3 and 74.6 eV reported for metallic platinum in the zerovalent state (Pt^0).[62−64] For Pt^{2+}, as in PtO and $Pt(OH)_2$, the Pt 4f doublet is known to be shifted by about +1.1 eV to 72.3 and 75.7 eV.[62−65] Thus, the more dominant doublet peaks appearing at slightly higher binding energies (72.3 and 76.2 eV) in the deconvoluted spectrum shown in Figure 7A can be assigned to Pt^{2+}. Finally, the third and weakest doublet component found in the spectrum at 74.8 and 78.0 eV can be ascribed to the Pt^{4+} oxidation state (as in PtO_2); these values are in close agreement with the observed binding energies of 74.2 and 77.5 eV reported by others for Pt^{4+}.[62,63] Overall, the deconvoluted XPS data support our contention that at least some reduction of the Pt^{2+} ion species to give zerovalent Pt metal occurred inside the PAMAM-OH dendrimers upon addition of sodium borohydride. Moreover, the presence of three distinct Pt 4f species, an observation which has not been reported in any previous XPS studies of Pt-DENs,[27,66] is interesting and suggests that perhaps residual, partially reduced Pt ion species (e.g., PtO, $Pt(OH)_2$, and/or PtO_2) are capping the surface of the nanoparticle metal core, or complexed within the PAMAM-OH dendrimer interior.

XPS analyses of the Pt-DENs also provided more detailed information about the chemical bonding structure of the nitrogen component that was not readily obtainable from the lower-energy resolution EELS spectra. Figure 7B shows the high-resolution N 1s spectrum that was acquired for a sample of Pt-DENs dried on a silicon wafer substrate. Whereas a relatively strong peak occurring in the region around 398−401 eV is seen for the Pt-DEN-containing sample, a control scan of the bare silicon substrate surface (Figure S2B) did not indicate the

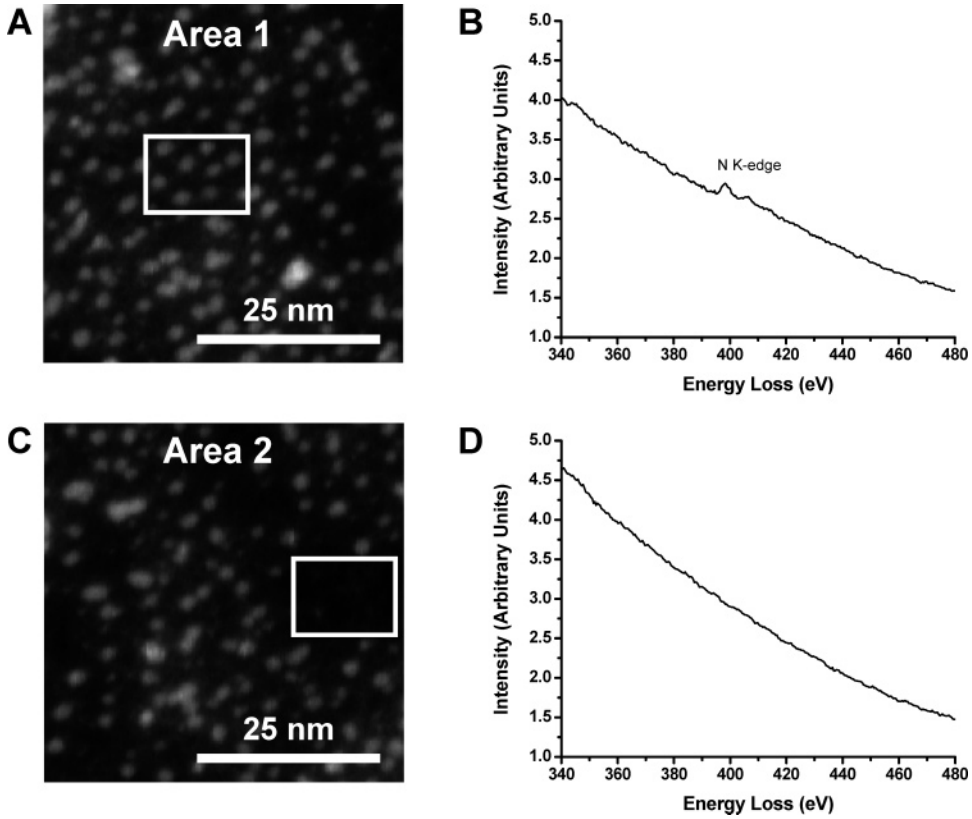

Figure 6. Electron energy loss spectroscopy (EELS) analysis of dendrimer-encapsulated platinum nanoparticles (Pt-DENs). A. Dark field STEM image of the Pt-DENs taken from one region (area 1) of the sample grid. B. EELS spectrum taken from the area outlined by the white box in A. The spectrum shows the characteristic feature at ~399 eV corresponding to the *K*-shell ionization edge of nitrogen (N K-edge). C. Dark field STEM image of the Pt-DENs taken from a different region (area 2) of the same sample grid analyzed in A. D. EELS spectrum taken from the grid background area outlined by the white box in C. The N *K* edge feature is absent from the spectrum.

presence of any significant nitrogen peaks due to, for example, adventitious contamination. Upon performing a deconvolution analysis of the spectrum in Figure 7B, we found that the experimental N 1s peak for the Pt-DEN sample can be modeled as the sum of two individual peaks occurring at binding energies of 398.7 and 400.1 eV. The peak at 398.7 eV can be ascribed to the presence of tertiary amine group nitrogens, which have been reported to have binding energies of around 399.0−399.1 eV.[67,68] On the other hand, the peak at 400.1 eV is consistent with the range of binding energies previously reported for amide-type nitrogens (i.e., 399.8−400.7 eV[69,70]). Significantly, the ratio of the peak areas ($peak_{400\ eV}$:$peak_{387.7\ eV}$ = 1.8:1) is quite close to the theoretical value of 2 expected for a PAMAM-OH dendrimer, whose ideal structure contains 124 amide nitrogens and 64 tertiary amine groups. Taken together, these N 1s XPS data thus provide additional supporting evidence that the Pt-DENs contain an organic dendrimer shell.

3.2. Bionanofabrication of Ordered Dendrimer-Encapsulated Platinum Nanoparticle Arrays Using S Layers. The ability to vary the interspacing between periodic features over very small distances (<50 nm) would make nanoparticle arrays particularly attractive for investigating the effects of nanoscale ordering on, for example, the optoelectronic and/or catalytic properties of materials. However, the efficient synthesis of well-ordered, 2-D arrays of target structures with nanometric lateral spacings remains a significant challenge. With this in mind, we next investigated the use of S layers as a biotemplate to pattern the dendrimer-stabilized platinum nanocomposite particles into organized structures. In light of the successes of other groups who have previously demonstrated the formation of metallic nanoparticle films via hydrogen bonding-based attractions,[71,72] our approach here was to use the numerous hydrogen-bonding active amide and hydroxyl groups found within the structure of the PAMAM-OH dendrimers as "molecular handles" to guide the self-assembly of the Pt-DENs onto different types of S-layer proteins pre-immobilized on TEM grid substrates. For these experiments, we generally expected that the periodically arranged functional groups located within the solvent-exposed regions of the native S layers could potentially serve as highly localized anchoring centers for the site-specific adsorption of incoming nanoparticles.

The first set of nanoparticle biotemplating experiments was conducted at pH 7 using the SAS S layer. TEM analyses showed that while the number of nanoparticles nonspecifically adsorbed to the bare surface of the TEM grid background (Figure 8A-(ii)) was nonzero (2290 ± 460 particles μm^{-2}), a significantly higher amount of particle binding was found in the areas of the grid containing S layers (6300 ± 370 particles μm^{-2}) (Figure 8A(i) and Table 1). At several locations, some of the S-layer-bound Pt-DENs appear to be aggregated together forming small clusters comprised of 2−3 closely spaced particles (with <2 nm interparticle edge-to-edge distance within each cluster). Furthermore, at least some visual indication of a higher level of ordering of the nanoparticles is readily discernible; more specifically, the individual Pt-DENs, as well as the small dimeric/trimeric clusters of Pt-DENs, appear to form a regular hexagonal pattern on the surface of the SAS template. The presence of an ordered nanoparticle pattern in the bright field TEM image shown in Figure 8A(i) is emphasized by the corresponding fast Fourier transform (FFT) power spectrum (inset to Figure 8A(i)), which shows a set of distinct peak reflections arranged in a 6-fold symmetry pattern. Moreover,

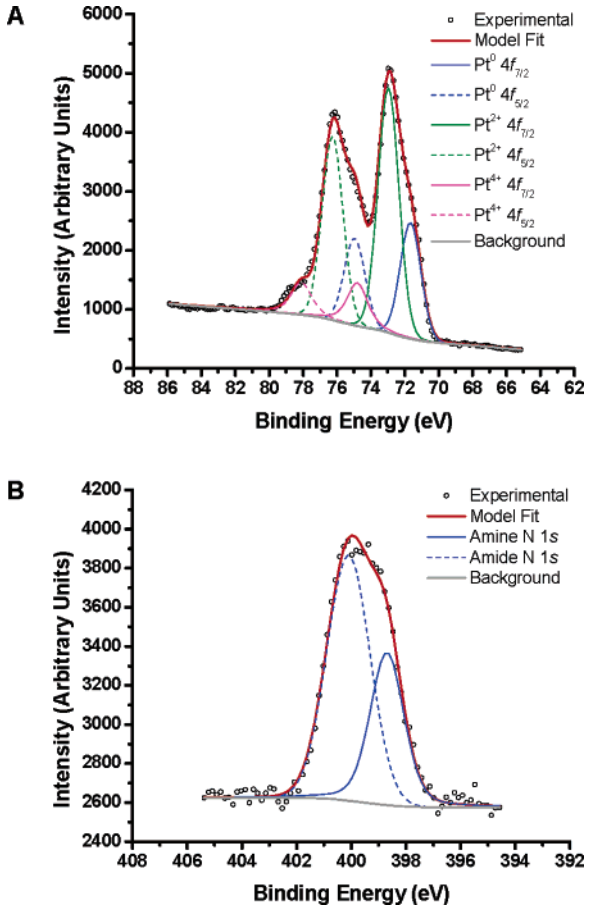

Figure 7. Core level XPS spectra of dendrimer-encapsulated nanoparticles deposited on a silicon (100) wafer substrate. A. Pt 4f region of the high-resolution XPS spectrum. The spectrum has been decomposed into 3 pairs of Pt $4f_{7/2}$ and Pt $4f_{5/2}$ spin−orbit doublets ($\chi^2 = 1.9$). B. N 1s region of the high-resolution XPS spectrum. The spectrum has been decomposed into two components corresponding to the N 1s signals from the amine-type nitrogens and the amide-type nitrogens ($\chi^2 = 0.5$).

the mean $d_{\{10\}}$-spacing value (see Figure S3 in the Supporting Information) of 18.7 ± 0.4 nm for the six {10} first-order peaks in the FFT plot further demonstrates that the Pt-DENs are arrayed with an overall periodicity (21.6 ± 0.4 nm = $2d_{\{10\}}/\sqrt{3}$) that is consistent with the reported lattice constant of the native SAS S-layer protein.

Taken together, the overall hexagonal-shaped ordering of the nanoparticle array and the formation of similar-sized dimeric/trimeric clusters strongly suggests that the Pt-DENs are adsorbed mainly within the vertex regions of the SAS protein. More specifically, we propose that the Pt-DENs are most likely bound within the large vertex (LV) regions of the SAS S layer, since the physical dimensions of this particular vertex location (diameter = 11.4 ± 0.5 nm; cf. schematic of the morphological structure of SAS S layer shown in Figure 2B) would appear to be sufficiently wide enough to accommodate the binding of more than just a single particle (theoretical PAMAM dendrimer diameter = 4.5 nm).[49] Thus, in this binding model, the topography and charge properties of the SAS S-layer surface initially serve to guide the deposition of the nanoparticles within the vertex areas of the protein template. Upon binding to these specific areas of the protein substrate, the Pt-DENs become physically confined and are held in place mainly through favorable noncovalent interactions (e.g., hydrogen bonding attractions and/or other types of van der Waals forces). Interestingly, a similar type of patterning of trimeric particle clusters on the SAS S layer has recently been observed by us[44] for water soluble CdSe/ZnS core−shell quantum dots.

Complementary Pt-DEN adsorption studies were subsequently performed using the HPI S layer in order to evaluate the effect of using different S-layer biotemplates for nanoparticle patterning. In these experiments, conducted at pH 7, the amount of nanoparticles nonspecifically adsorbed to S-layer-free areas of the TEM grid surface (Figure 8B(ii)) was again relatively low (2180 ± 360 particles μm^{-2}). In stark contrast to their appearance on the SAS S layer, however, the surface coverage density of the Pt-DEN particles deposited on the HPI protein template is much higher (12 690 ± 990 particles μm^{-2}) (Figure 8B(i) and Table 1). Moreover, the particles are strikingly arranged into a hollow hexagonal or "honeycomb" pattern. In this case, a variable number of the Pt-DENs (typically 6−12 individual particles) appear to pack together to form well-defined, ring-type structures within the nanoparticle array. Close examination of the bright field TEM image suggests that the nearest-neighbor (center-to-center) distance between adjacent particles within the ring-type structures ranges from approximately 4−10 nm. The strong peak reflections found in the corresponding fast Fourier transform plot (inset to Figure 8B-(i)) confirm that the Pt-DEN array has a mostly 6-fold orientational symmetry. Furthermore, the measured $d_{\{10\}}$-spacing value of 15.9 ± 0.2 nm provides additional evidence that the Pt-DENs are arranged with a dominant periodicity (18.3 ± 0.2 nm) commensurate with the reported lattice constant of the native HPI S-layer protein. The relatively dense, honeycomb-ordered packing of the individual particles on the HPI template likely arises from a high intrinsic affinity between the dendrimer component of the Pt-DENs and various polar/charged functional groups located within the vertex regions of the S-layer protein monolayer.

Overall, the preceding results clearly demonstrate that different geometric patterns of nanoparticle assemblies are formed depending on which particular type of S-layer substrate interfacial structure is present. Although the degree of uniformity of the hexagonal-/honeycomb-ordering seen in the fabricated Pt-DEN arrays is obviously less than perfect, the results presented here are an encouraging step toward the controlled nanoscale 2-D patterning of dendrimer−metal nanocomposite materials using a simple biological templating-based approach. Furthermore, it seems likely that the creation of long-range ordered arrays displaying a more highly uniform appearance may eventually be achievable through several possible routes, including (1) optimization of the relevant solution deposition conditions affecting particle binding on the S layers (e.g., temperature, ionic strength, Pt-DEN concentration, etc.), (2) optimization of the Pt-DEN synthesis conditions to achieve a higher level of particle monodispersity, and (3) exploitation of novel protein engineering techniques (e.g., incorporation of "unnatural" amino acids[73] into S-layer proteins) for improved site-specific binding of functionalized nanoparticles.

Interestingly, under a fixed set of experimental conditions, only a single type of Pt-DEN array pattern is typically observed for each species of protein biotemplate employed, even though the intracellular and extracellular surfaces of the HPI and SAS S layers have been shown to display different topological properties.[44] In any case, the results described above provide further evidence in support of the finding by others[74,75] that the use of hydroxyl-terminated PAMAM dendrimers, which have a decreased number of protonated amine sites relative to the other types of ("conventional") primary amine-terminated

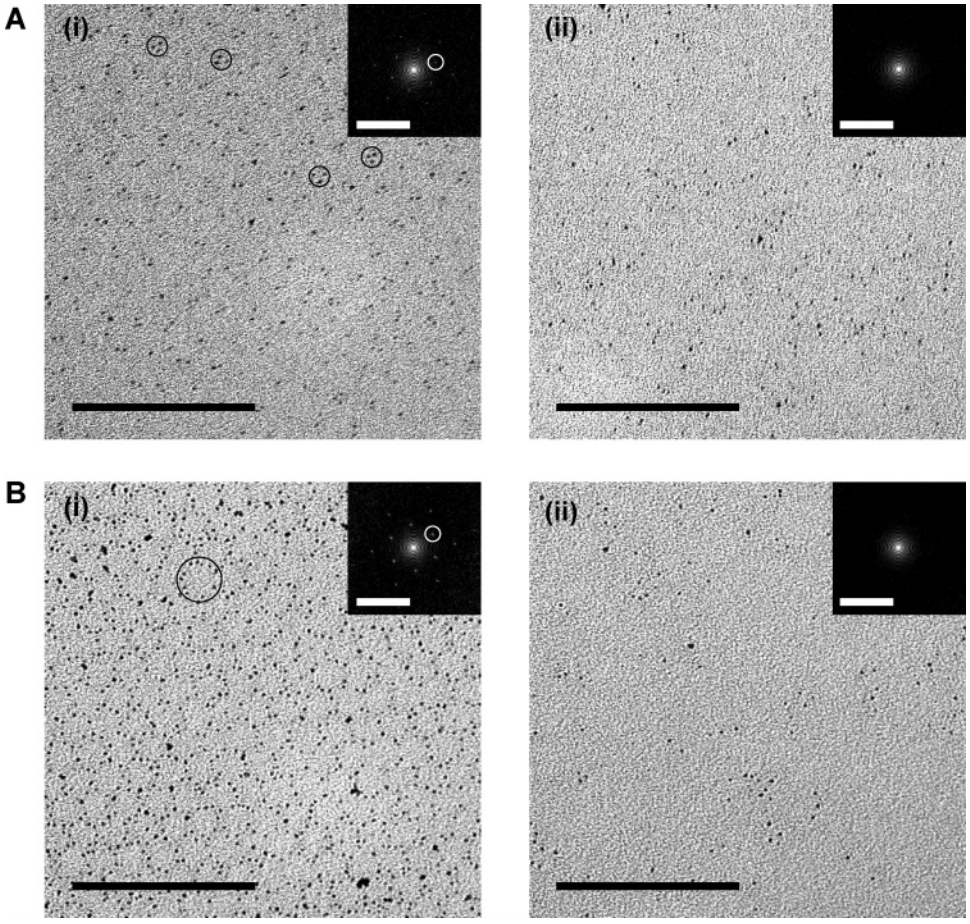

Figure 8. Brightfield TEM images and corresponding 2-D FFT power spectra of unstained S layers after incubation in dendrimer-encapsulated platinum nanoparticle (Pt-DEN) solutions at pH 7. A. Pt-DENs biotemplated on the SAS S layer at pH 7: (i) TEM image of a region of the grid containing SAS S layers. Black circles mark examples of trimeric clusters of nanoparticles. (ii) TEM image of a region of the grid without any SAS S layers present. B. Pt-DENs biotemplated on the HPI S layer at pH 7: (i) TEM image of a region of the grid containing HPI S layers. Black circle marks an example of a ring-type structure formed by a group of 11 individual nanoparticles. (ii) TEM image of a region of the grid without any HPI S layers present. For all TEM images, scale bar = 100 nm. For all FFT spectra, scale bar = 0.15 nm^{-1}. All FFT spectra were calculated for a 305 nm-diameter circular region of the pattern. In the FFT plots shown in A(i) and B(i), the white circle marks a representative diffraction spot which can be indexed to the (10) lattice line found in a (hypothetical) 2-D hexagonal/honeycomb array structure.

Table 1. Number of Nanoparticles (Pt-DENs) Adsorbed onto HPI and SAS S Layers under Different Buffer pH Conditions[a]

S layer	pH 5 (particles μm^{-2})	pH 7 (particles μm^{-2})	pH 9 (particles μm^{-2})
SAS	15540 ± 1620	6300 ± 370	5410 ± 340
HPI	21070 ± 2770	12600 ± 990	8250 ± 690

[a] Data presented are mean ± standard deviation values calculated from a minimum of 4 nonoverlapping regions of interest (ROIs) (sample area size for each ROI = 238 × 238 nm).

dendrimers, does not in any way compromise the ability to fabricate thin-film assemblies of the dendrimers on planar supports. High-generation PAMAM-OH dendrimers, such as the generation 4 dendrimers that were used in the present work, obviously contain numerous amide and hydroxyl groups that can participate in hydrogen bonding interactions with target substrates. In general, such types of nonelectrostatic-based interactions can be quite strong because a relatively large number of hydrogen bonds can form per dendrimer molecule. On the other hand, it seems entirely reasonable that under appropriate conditions, the dendrimer interior (tertiary) amines, when protonated, could also serve to provide a source of charged groups for an alternative electrostatic-based adsorption mechanism. Sun and Crooks,[74] for example, have shown that generation 6 PAMAM dendrimers with hydroxyl terminal groups can become strongly adsorbed onto freshly cleaved muscovite mica surfaces. This interaction could be attributed to two likely sources:[75] (1) hydrogen bonding-based attractions between functional groups on the PAMAM dendrimer and hydroxyl groups on the hydrophilic mica surface and (2) electrostatic-based attractions between positively charged tertiary amine groups within the PAMAM-OH dendrimer and the negative aluminosilicate lattice charges in the mica crystal structure.

To explore further the mechanism of adsorption of Pt-DENs on the S-layer templates, additional experiments were performed to investigate the effect of different pH buffer conditions on nanoparticle array formation. Within the primary structure of both HPI and SAS, numerous functional groups are present which will have different ionization states depending on the pH of the solution environment. Changes in the protonation state of amino acids located on the surface of an S layer could, in turn, potentially affect the interactions between the protein and the Pt-DENs. In addition, it is generally known that pH can influence a polymer's ability to undergo hydrogen bond (H-bond) interactions; OH^- ions in solution, for example, can act to dissociate hydrogen bonds under basic pH conditions.[76] Moreover, although it is unlikely that the hydroxyl groups found on the outermost surface of the PAMAM-OH dendrimers used in this work can undergo any significant level of protonation

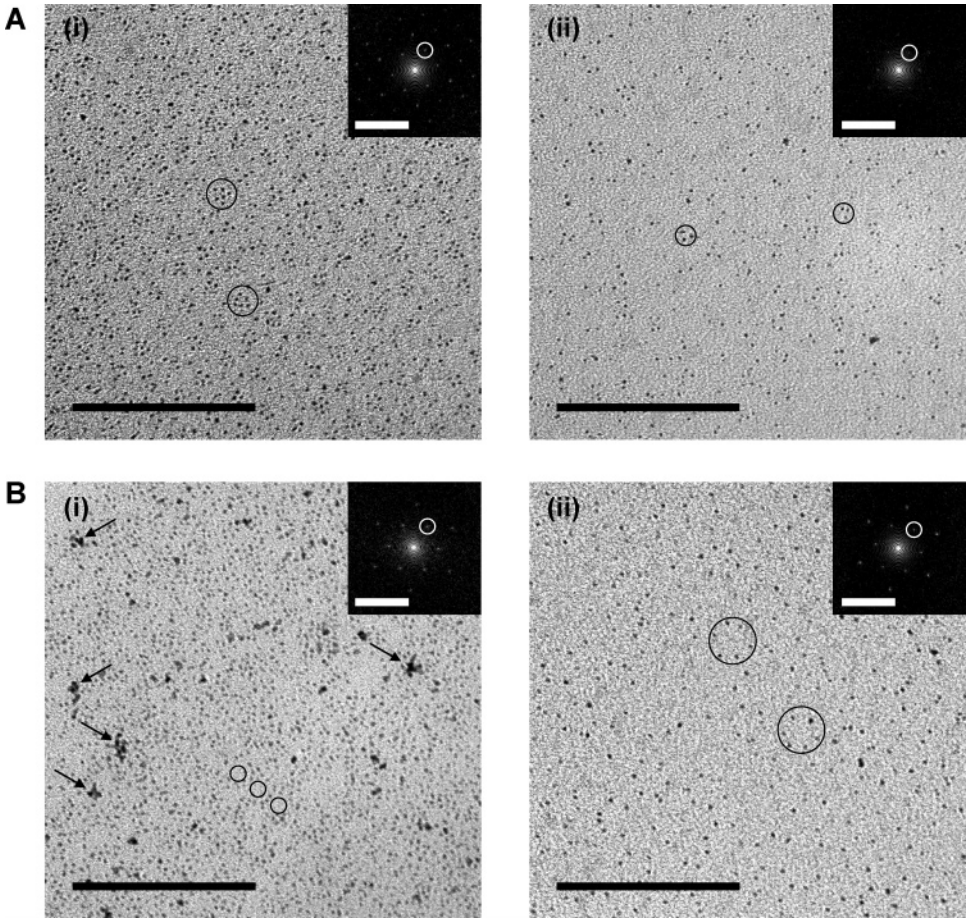

Figure 9. Brightfield TEM images and corresponding 2-D FFT power spectra of unstained S layers after incubation in dendrimer-encapsulated platinum nanoparticle (Pt-DEN) solutions at pH 5 and pH 9. A. Pt-DENs biotemplated on the SAS S layer: (i) Pt-DENs biotemplated on the SAS S layer at pH 5. Black circles mark examples of hexameric clusters of nanoparticles. (ii) Pt-DENs biotemplated on the SAS S layer at pH 9. Black circles mark examples of trimeric clusters of nanoparticles. B. Pt-DENs biotemplated on the HPI S layer: (i) Pt-DENs biotemplated on the HPI S layer at pH 5. Black circles mark examples of "pockets" of bare (particle-free) areas of the nanopatterned surface. Black arrows point to examples of randomly aggregated clusters of nanoparticles. (ii) Pt-DENs biotemplated on the HPI S layer at pH 9. Black circles mark examples of hexagonally arranged clusters comprised of a group of 6 individual nanoparticles. For all TEM images, scale bar = 100 nm. For all FFT spectra, scale bar = 0.15 nm^{-1}. All FFT spectra were calculated for a 305 nm-diameter circular region of the pattern. In the FFT plots, the white circle marks a representative diffraction spot which can be indexed to the (10) lattice line found in a (hypothetical) 2-D hexagonal/honeycomb array structure.

under mildly acidic conditions to form oxonium ions, it has been reported that the interior PAMAM tertiary amines (with measured pK_a values[77−79] in the range of ∼6.3−6.6) can become protonated under buffer conditions in the pH range 3−6.[80] Conversely, it is known that a minimal number of these tertiary amines are protonated under pH conditions above 8.[80] And finally, other studies[81] have further shown that the Coulombic repulsion of charged tertiary amine groups of the inner dendrimer shells under acidic pH conditions leads to a more fully extended structure and hence an increase of the dendrimer hydrodynamic radius. For all of the above reasons, we thus presumed that the overall ionization state of these tertiary amine groups, some of which are localized very close (<1 nm) to the outermost surface of the dendrimer molecule, could also influence the adsorption behavior of the dendrimer-encapsulated nanoparticles on the S layers.

Figure 9 shows representative TEM images of the Pt-DENs adsorbed onto the HPI and SAS S layers under acidic and basic pH conditions. At pH 5, the overall surface coverage of bound nanoparticles appeared to increase significantly for both types of S layers. In the case of SAS, the Pt-DENs were found to adsorb at a surface density of 15 540 ± 1620 particles μm^{-2}, close to 2.5 times the surface coverage value observed under neutral pH conditions (cf. Table 1). Initially, the nanoparticles seen in the TEM image (Figure 9A(i)) appear to be relatively disordered on the SAS surface. In fact, however, a systemic clustering of the Pt-DENs (into groups of ∼3−7 particles) on the S layer is still visually discernible; this is more clearly evident when the TEM image is viewed by eye at a low angle from several directions. Moreover, the corresponding FFT spectrum (inset to Figure 9A(i)) provides further evidence indicating that an underlying hexagonal symmetry dominates the image. From the FFT plot, the measured $d_{\{10\}}$-spacing value of 18.4 ± 0.7 nm verifies that the Pt-DENs are indeed regularly arrayed with an overall periodicity (21.3 ± 0.8 nm) that closely corresponds to the lattice constant of the SAS S layer.

In the case of the HPI S layer, adsorption of the Pt-DENs at pH 5 resulted in a surface coverage of 21 070 ± 2770 particles μm^{-2}. Interestingly, under these acidic buffer conditions, there appeared to be an increased level of random (bulk) aggregation of the nanoparticles on the S layer (Figure 9B(i)), compared to when the experiments were carried out at pH 7 (cf. Figure 8B-(i)). For the most part, the randomly aggregated appearance of some of the HPI S-layer-bound dendrimer-metal particles was unexpected, since nonspecific aggregation effects due to intermolecular hydrogen-bonding between peripheral OH groups of

PAMAM dendrimers are not typically encountered under the concentration and pH conditions used here. Despite the frequent occurrence of these nonspecifically aggregated clusters, the nanoparticles appear to collectively maintain at least some of the honeycomb-type ordering previously observed at neutral pH conditions. In this case, however, the individual Pt-DENs are no longer spatially constrained within narrow, ring-type structures; instead, most of the particles seem to be dispersed into loosely organized groupings that surround small "pockets" of particle-free regions on the S-layer surface (Figure 9B(i)). Close inspection of the corresponding FFT spectrum again confirms the presence of a 6-fold orientational symmetry in the nanoparticle pattern (inset to Figure 9B(i)), consistent with the morphological structure of the HPI template. Finally, the mean $d_{\{10\}}$-spacing value of 15.8 ± 0.1 nm obtained for the FFT indicates that the spatial periodicity (18.3 ± 0.1 nm) of the features found in the TEM image is in good agreement with the measured lattice constant of the native HPI protein

When the biotemplating experiments were conducted at pH 9, TEM analyses of the HPI and SAS S layers indicated that the overall amount of nanoparticle binding on both protein templates was decreased compared to the levels of binding seen at either neutral or acidic pH conditions (Table 1). In the case of the SAS S layer, the calculated surface density of the Pt-DENs at pH 9 is found to be 5410 ± 340 particles μm^{-2}. Although similar types of adsorbed dimeric/trimeric Pt-DEN clusters are seen under both pH 7 and 9 buffer conditions, the interaction of the particles with the surface of the SAS protein at pH 9 (Figure 9A(ii)) results in an adsorption pattern that visually appears less well-ordered than that obtained at pH 7 (cf. Figure 8A(i)). The accompanying FFT spectrum (inset to Figure 9A(ii)) for the pH 9 adsorption pattern, on the other hand, demonstrates that the Pt-DENs are in fact organized into a hexagonally ordered 2-D assembly on the SAS template with a feature periodicity of 21.6 ± 0.3 nm ($d_{\{10\}}$-spacing = 18.7 ± 0.2 nm).

For the HPI S layer, adsorption of the Pt-DENs at pH 9 was found to lead to the formation of a visually identifiable "quasihoneycomb" pattern comprised of an array of mostly incomplete hexagonal unit cells containing a variable number of dendrimer-stabilized particles spaced ~10−12 nm apart (interparticle center-to-center spacing; Figure 9B(ii)). The empirically determined surface coverage of the nanoparticles under these basic pH conditions is 8250 ± 690 particles μm^{-2}, roughly 1.5 times less than that calculated for the honeycomb-structured arrays formed at pH 7. Examination of the inset FFT plot for the TEM image shown in Figure 9B(ii) verifies the presence of an ordered lattice structure having a 6-fold symmetry. In addition, the $d_{\{10\}}$-spacing value of 15.8 ± 0.2 nm calculated from the FFT spectrum clearly indicates that the overall periodicity of the quasihoneycomb array (18.2 ± 0.2 nm) is in excellent agreement with the HPI S-layer lattice constant.

It is obvious that any particular combination of several factors may be contributing to the observed pH-induced changes in the adsorption behavior of the Pt-DENs on the S layers. As already mentioned earlier, possibilities include the development of at least some electrostatic charge on the PAMAM dendrimers due to a weak level of protonation of the internal tertiary amines, as well as the ionization of various functional groups on the S layers themselves. Under conditions of pH 5, the denser packing (and/or increased aggregation) of the nanoparticles on the S layers may be due to protein-induced bridging mediated by electrostatic attractions in combination with other noncovalent interactions occurring between functional groups on the S-layer template and the partially charged PAMAM dendrimers. In contrast, when the pH of the Pt-DEN solution is raised to pH 9 (i.e., increased concentration of OH^- ions), the overall decreased amount of surface coverage by the particles could be the result of the development of weaker hydrogen bonds due to the greater degree of deprotonation and/or ionization of H-bond donor groups in the S-layer protein structure.

Unfortunately, the lack of any high-resolution 3-D structural data and very limited information[47] about the physical/biochemical characteristics of the HPI and SAS S layers make it difficult to determine the precise origin of the pH effects described above. Close inspection of the reported nucleotide sequence of the gene encoding the HPI S layer[82] reveals that the mature polypeptide (98 kDa) contains 24 lysine residues (2.6 mol %), 42 arginine residues (4.5 mol %), 57 aspartic acid residues (6.1 mol %), and 24 glutamic acid residues (2.6 mol %). Along similar lines, an early biochemical investigation of the SAS S layer[50] (whose corresponding gene has yet to be identified) has shown that this polypeptide contains 2.20 ± 0.04 mol % lysine, 0.30 ± 0.03 mol % arginine, 9.3 ± 0.3 mol % aspartic acid, and 6.6 ± 0.5 mol % glutamic acid. These amino acid compositional data emphasize the fact that for both HPI and SAS there are indeed significant numbers of positively and negatively charged residues that are potentially available to influence the binding of the Pt-DENs under the various solution conditions used in our biotemplating experiments. On the other hand, because of the lack of detailed knowledge of the atomic structure of these proteins, it is not possible at this time to ascertain which particular S-layer amino acids are exposed to solvent and are therefore likely candidates for interactions with the dendrimer−metal complexes. Once atomic-resolution 3-D structures do become available, however, it should be extremely interesting in future studies to perform protein engineering experiments to evaluate the effects of introducing site-specific point mutations in the S layers. In any case, the empirical results described in this article suggest that for the Pt-DENs, solution conditions near neutral pH values appear to be the most optimal for the biotemplated synthesis of hexagonal- and honeycomb-ordered nanoparticle array structures using these microbial S-layer proteins. It can be anticipated, however, that a tighter level of control over particle/S-layer interactions − and thus an enhanced uniformity of patterning − may be achievable by using alternative PAMAM dendrimer host systems with novel types of chemically tailored functional groups.

4. Conclusion

The key result of the work presented in this article is the demonstration of a simple, biotemplate-based approach for the fabrication of nanoarrays using well-characterized dendrimer-encapsulated platinum nanoparticles in conjunction with microbial S-layer protein lattices displaying highly periodic chemical and topographic properties. Unlike most other 2-D self-assembly methods which afford only random, close-packed and/or nonuniform structures, we have shown that by using the S layers from *S. acidocaldarius* and *D. radiodurans* as a biomolecular template, spatially ordered arrays of dendrimer-encapsulated metallic particles with a nanometric lateral pitch could be fabricated via noncovalent bonding forces without the need for any complicated lithographic/thin-film processing steps.

The possibility of achieving controlled nanoparticle growth by utilizing dendrimer-based templates has the great advantage of permitting the synthesis of well-dispersed metal clusters in

aqueous solution while allowing for a metallization procedure that remains very simple and which does not require the use of environmentally problematic organic solvents. When combined with the nanostructuring properties afforded by the use of S-layer-based protein templates, this opens the way for a wide range of applications in nanotechnology. Clearly, the development of effective patterning methods to control particle assembly on a nanometer scale is an essential step toward technologies that aim to integrate nanoarrays as part of functional device structures.[83] Our next step is to conduct further characterization studies of platinum nanoparticle arrays synthesized on silicon substrates in order to better understand the physical/chemical properties of these materials and to assess their potential as 2-D model supported nanocatalyst systems. In addition, biotemplating investigations using other types of monometallic/bimetallic DENs and S layers are currently in progress.

Acknowledgment. The authors thank Dr. Aaron D. Strickland for insightful discussions regarding PAMAM dendrimer chemistry. Malcolm G. Thomas is gratefully acknowledged for providing outstanding technical assistance with the UHV-STEM/EELS analyses. We also thank John Grazul for his excellent technical assistance with the HRTEM analyses. This work was supported in part by the Nanobiotechnology Center (NBTC), an STC Program of the National Science Foundation under Agreement Number ECS-9876771. We also acknowledge additional funding support from the National Science Foundation under a Nanoscale Interdisciplinary Research Team (NIRT) grant (NSF-0403990). Finally, we note that this work made use of the Cornell Center for Materials Research (CCMR) Facilities supported by the National Science Foundation under Award Number DMR-0520404.

Supporting Information Available. Figure S1 (chemical structure of a generation 4 PAMAM dendrimer bearing 64 surface hydroxyl groups), Figure S2 (XPS spectra obtained for a "blank" Si(100) wafer substrate), and Figure S3 (schematic illustration of the major lattice orientations in an ideal 2-D hexagonal array structure). This material is available free of charge via the Internet at http://pubs.acs.org.

References and Notes

(1) Modrow, H.; Modrow, S.; Hormes, J.; Waldofner, N.; Bonnemann, H. *J. Phys. Chem. B* **2005**, *109*, 900−906.
(2) Cheyne, R. B.; Moffitt, M. G. *Langmuir* **2005**, *21*, 10297−10300.
(3) Shao, M.-H.; Sasaki, K.; Adzic, R. R. *J. Am. Chem. Soc.* **2006**, *128*, 3526−3527.
(4) Sun, E. Y.; Josephson, L.; Kelly, K. A.; Weissleder, R. *Bioconjugate Chem.* **2006**, *17*, 109−113.
(5) Kawasaki, M.; Hori, M. *J. Phys. Chem. B* **2003**, *107*, 6760−6765.
(6) Sun, Z.; Kim, D. H.; Wolkenhauer, M.; Bumbu, G. G.; Knoll, W.; Gutmann, J. S. *ChemPhysChem* **2006**, *7*, 370−378.
(7) Wang, S.; Kang, S. S.; Nikles, D. E.; Harrell, J. W.; Wu, X. W. *J. Magn. Magn. Mater.* **2003**, *266*, 49−56.
(8) Xia, D.; Brueck, S. R. J. *Nano Lett.* **2004**, *4*, 1295−1299.
(9) Grunes, J.; Zhu, J.; Anderson, E. A.; Somorjai, G. A. *J. Phys. Chem. B* **2002**, *106*, 11463−11468.
(10) Liu, X.; Fu, L.; Hong, S.; Dravid, V. P.; Mirkin, C. A. *Adv. Mater.* **2002**, 14.
(11) Pinto, Y. Y. L., J. D.; Seeman, N. C.; Musier-Forsyth, K.; Taton, T. A.; Kiehl, R. A. *Nano Lett.* **2005**, *5*, 2399−2402.
(12) McMillan, R. A.; Howard, J.; Zaluzec, N. J.; Kagawa, H. K.; Mogul, R.; Li, Y.-F.; Paavola, C. D.; Trent, J. D. *J. Am. Chem. Soc.* **2005**, *127*, 2800−2801.
(13) Sleytr, U. B. S., M.; Pum, D.; Schuster, B. *Prog. Surf. Sci.* **2001**, *68*, 231−278.
(14) Sara, M.; Pum, D.; Schuster, B.; Sleytr, U. B. *J. Nanosci. Nanotechnol.* **2005**, *5*, 1939−1953.
(15) Shenton, W.; Pum, D.; Sleytr, U. B.; Mann, S. *Nature* **1997**, *389*, 585−587.
(16) Mertig, M.; Kirsch, R.; Pompe, W.; Engelhardt, H. *Eur. Phys. J. D* **1999**, *9*, 45−48.
(17) Mertig, M.; Wahl, R.; Lehmann, M.; Simon, P.; Pompe, W. *Eur. Phys. J. D* **2001**, *16*, 317−320.
(18) Vyalikh, D. V.; Danzenbacher, S.; Mertig, M.; Kirchner, A.; Pompe, W.; Dedkov, Y. S.; Molodtsov, S. L. *Phys. Rev. Lett.* **2004**, *93*, 238103/1−238103/4.
(19) Tomalia, D. A.; Naylor, A. M.; Goddard, W. A., III *Angew. Chem., Int. Ed.* **1990**, *29*, 138−175.
(20) Esfand, R.; Tomalia, D. A. *Drug Discovery Today* **2001**, *6*, 427−436.
(21) Tomalia, D. A. *Mater. Today* **2005**, *8*, 34−46.
(22) Crooks, R. M. L.; Buford, I., III.; Sun, Li; Yeung, L. K.; Zhao, M. *Top. Curr. Chem.* **2001**, *212*, 81−135.
(23) Esumi, K. *Top. Curr. Chem.* **2003**, *227*, 31−52.
(24) Scott, R. W. J.; Wilson, O. M.; Crooks, R. M. *J. Phys. Chem. B* **2005**, *109*, 692−704.
(25) Bronstein, L. M.; Sidorov, S. N.; Valetsky, P. M. *Russ. Chem. Rev.* **2004**, *73*, 501−515.
(26) Crooks, R. M.; Zhao, M.; Sun, L.; Chechik, V.; Yeung, L. K. *Acc. Chem. Res.* **2001**, *34*, 181−190.
(27) Zhao, M.; Crooks, R. M. *Angew. Chem., Int. Ed.* **1999**, *38*, 364−366.
(28) Zhao, M.; Crooks, R. M. *Adv. Mater.* **1999**, *11*, 217−220.
(29) Ye, H.; Scott, R. W. J.; Crooks, R. M. *Langmuir* **2004**, *20*, 2915−2920.
(30) You, T.; Niwa, O.; Tomita, M.; Hirono, S. *Anal. Chem.* **2003**, *75*, 2080−2085.
(31) Lu, S.; Panchapakesan, B. *Nanotech.* **2006**, *17*, 888−894.
(32) Zhu, J.; Somorjai, G. A. *Nano Lett.* **2001**, *1*, 8−13.
(33) Grunes, J.; Zhu, J.; Yang, M.; Somorjai, G. A. *Catal. Lett.* **2003**, *86*, 157−161.
(34) Lin, Y.; Cui, X.; Yen, C.; Wai, C. M. *J. Phys. Chem. B* **2005**, *109*, 14410−14415.
(35) Kapoor, S.; Belapurkar, A. D.; Mittal, J. P.; Mukherjee, T. *Mater. Res. Bull.* **2005**, *40*, 1654−1661.
(36) Wells, M.; Crooks, R. M. *J. Am. Chem. Soc.* **1996**, *118*, 3988−3989.
(37) Tokuhisa, H.; Crooks, R. M. *Langmuir* **1997**, *13*, 5608−5612.
(38) Wang, J.; Jia, X.; Zhong, H.; Luo, Y.; Zhao, X.; Cao, W.; Li, M.; Wei, Y. *Chem. Mater.* **2002**, *14*, 2854−2858.
(39) Degenhart, G. H.; Dordi, B.; Schonherr, H.; Vancso, G. J. *Langmuir* **2004**, *20*, 6216−6224.
(40) Mark, S. S.; Sandhyarani, N.; Zhu, C.; Campagnolo, C.; Batt, C. A. *Langmuir* **2004**, *20*, 6808−6817.
(41) He, J. A.; Valluzzi, R.; Yang, K.; Dolukhanyan, T.; Sung, C.; Kumar, J.; Tripathy, S. K.; Samuelson, L.; Balogh, L.; Tomalia, D. A. *Chem. Mater.* **1999**, 11.
(42) Liu, Y.-C.; Chen, H.-L.; Lin, H.-K.; Liu, W.-L.; Chou, Y.-W.; Lo, S.-C.; Tai, C.-H. *Biomacromolecules* **2005**, *6*, 3481−3485.
(43) Zhong, H.; Wang, J.; Jia, X.; Li, Y.; Qin, Y.; Chen, J.; Zhao, X. S.; Cao, W.; Li, M.; Wei, Y. *Macromol. Rapid. Commun.* **2001**, *22*, 583−586.
(44) Mark, S. S.; Bergkvist, M.; Yang, X.; Teixeira, L. M.; Bhatnagar, P.; Angert, E. R.; Batt, C. A. *Langmuir* **2006**, *22*, 3763−3774.
(45) Baumeister, W.; Barth, M.; Hegerl, R.; Guckenberger, R.; Hahn, M.; Saxton, W. O. *J. Mol. Biol.* **1986**, *187*, 241−250.
(46) Hall, S. R.; Shenton, W.; Engelhardt, H.; Mann, S. *ChemPhysChem* **2001**, *2*, 184−186.
(47) Bergkvist, M.; Mark, S. S.; Yang, X.; Angert, E. R.; Batt, C. A. *J. Phys. Chem. B* **2004**, *108*, 8241−8248.
(48) Devaud, G.; Furcinitti, P. S.; Fleming, J. C.; Lyon, M. K.; Douglas, K. *Biophys. J.* **1992**, *63*, 630−638.
(49) Hierlemann, A.; Campbell, J. K.; Baker, L. A.; Crooks, R. M.; Ricco, A. J. *J. Am. Chem. Soc.* **1998**, *120*, 5323−5324.
(50) Michel, H.; Neugebauer, D. C.; Oesterhelt, D. The 2-dimensional crystalline cell wall of Sulfolobus acidocaldarius: structure, solubilization, and reassembly. In *Electron Microscopy at Molecular Dimensions*; Baumeister, W., Vogell, W., Eds.; Springer: New York, 1980; pp 27−35.
(51) Shirley, D. A. *Phys. Rev. B* **1972**, *5*, 4709−4714.
(52) Lee, K.; Lee, K. H.; Ju, B. K.; Whang, C. N. *J. Korean Phys. Soc.* **2002**, *41*, 745−748.
(53) Bancroft, G. M.; Adams, I.; Coatsworth, L. L.; Bennewitz, C. D.; Brown, J. D.; Westwood, W. D. *Anal. Chem.* **1975**, *47*, 586−588.
(54) Fairley, N. XPS line shapes and curve fitting. In *Surface Analysis by Auger and X-ray Photoelectron Spectroscopy*; Briggs, D. G., John, T., Ed.; IM Publications: Chichester, U.K., 2003; pp 397-420.
(55) Cumpson, P. J.; Seah, M. P. *Surf. Interface Anal.* **1992**, *18*, 345−360.

(56) Crist, B. V. *Handbook of Monochromatic XPS Spectra*; John Wiley & Sons: New York, 2000.
(57) Yao, H.; Kojima, H.; Sato, S.; Kimura, K. *Langmuir* **2004**, *20*, 10317−10323.
(58) Pellechia, P. J.; Gao, J.; Gu, Y.; Ploehn, H. J.; Murphy, C. J. *Inorg. Chem.* **2004**, *43*, 1421−1428.
(59) Chen, J.; Herricks, T.; Geissler, M.; Xia, Y. *J. Am. Chem. Soc.* **2004**, *126*, 10854−10855.
(60) Xie, H.; Gu, Y.; Ploehn, H. J. *Nanotechnology* **2005**, *16*, 492−501.
(61) Statham, P. J. *Microsc. Microanal.* **1998**, *4*, 605−615.
(62) Chastain, J.; King, R. C. *Handbook of X-ray Photoelectron Spectroscopy*; Physical. Electronics, Inc.: Eden Prairie, MN, 1995.
(63) Whalen, J. J., III.; Weiland, J. D.; Searson, P. C. *J. Electrochem. Soc.* **2005**, *152*, C738−C743.
(64) Parkinson, C. R.; Walker, M.; McConville, C. F. *Surf. Sci.* **2003**, *545*, 19−33.
(65) Jung, M.-C.; Kim, H.-D.; Han, M.; Jo, W.; Kim, D. C. *Jpn. J. Appl. Phys.* **1999**, *38*, 4872−4875.
(66) Zhao, M.; Crooks, R. M. *Chem. Mater.* **1999**, *11*, 3379−3385.
(67) Liu, Y.; Goh, S. H.; Lee, S. Y.; Huan, C. H. A. *J. Polym. Sci., Part B: Polym. Phys.* **2000**, *38*, 501−508.
(68) Yu, Z. J.; Kang, E. T.; Neoh, K. G. *J. Electrochem. Soc.* **2002**, *149*, C10−C17.
(69) Zhang, X.; Bai, R. *J. Mater. Chem.* **2002**, *12*, 2733−2739.
(70) Wang, Y.; Lu, L.; Zheng, Y.; Chen, X. *J. Biomed. Mater. Res., Part A* **2006**, *76A*, 589−595.
(71) Mayer, C. R.; Neveu, S.; Secheresse, F.; Cabuil, V. *J. Colloid Interface Sci.* **2004**, *273*, 350−355.
(72) Zirbs, R.; Kienberger, F.; Hinterdorfer, P.; Binder, W. H. *Langmuir* **2005**, *21*, 8414−8421.
(73) Anderson, J. C.; Wu, N.; Santoro, S. W.; Lakshman, V.; King, D. S.; Schultz, P. G. *Proc. Natl. Acad. Sci.* **2004**, *101*, 7566−7571.
(74) Sun, L.; Crooks, R. M. *Langmuir* **2002**, *18*, 8231−8236.
(75) Sun, L.; Ca, D. V.; Cox, J. A. *J. Solid State Electrochem.* **2005**, *9*, 816−822.
(76) Stockton, W. B.; Rubner, M. F. *Macromolecules* **1997**, *30*, 2717−2725.
(77) Niu, Y.; Sun, L.; Crooks, R. M. *Macromolecules* **2003**, *36*, 5725−5731.
(78) Leisner, D.; Imae, T. *J. Phys. Chem. B* **2004**, *108*, 1798−1804.
(79) Krot, K. A.; Danil de Namor, A. F.; Aguilar-Cornejo, A.; Nolan, K. B. *Inorg. Chim. Acta* **2005**, *358*, 3497−3505.
(80) Kleinman, M. H.; Flory, J. H.; Tomalia, D. A.; Turro, N. J. *J. Phys. Chem. B* **2000**, *104*, 11472−11479.
(81) Castagnola, M.; Zuppi, C.; Rossetti, D. V.; Vincenzoni, F.; Lupi, A.; Vitali, A.; Meucci, E.; Messana, I. *Electrophoresis* **2002**, *23*, 1769−1778.
(82) Peters, J.; Peters, M.; Lottspeich, F.; Schäfer, W.; Baumeister, W. *J. Bacteriol.* **1987**, *169*, 5216−5223.
(83) Cui, Y.; Bjork, M. T.; Liddle, J. A.; Sonnichsen, C.; Boussert, B.; Alivisatos, A. P. *Nano Lett.* **2004**, *4*, 1093−1098.

BM0603185